A Monotone, Higher-Order Accurate, Fixed-Grid Finite-Volume Method for Advection Problems with Moving Boundaries[*]

Y. Hassen[1,2] and B. Koren[1,2]

[1] Centre for Mathematics and Computer Science
P.O.Box 94079, 1090 GB, Amsterdam, the Netherlands

[2] Faculty of Aerospace Engineering, TU Delft
P.O.Box 5058, 2600 GB, Delft, the Netherlands

e-mails: {*yunus.hassen, barry.koren*}@*cwi.nl*

Abstract

In this paper, an accurate method, using a novel immersed-boundary approach, is presented for numerically solving linear, scalar convection problems. As is standard in immersed-boundary methods, moving bodies are embedded in a fixed Cartesian grid. The essence of the present method is that specific fluxes in the vicinity of a moving body are computed in an intelligent way such that they accurately accommodate the boundary conditions valid on the moving body. The first results obtained are very accurate, without requiring much computational overhead. It is anticipated that the method can be easily and successfully extended to real fluid-flow equations.

1 Introduction

In this paper, we consider numerical solutions of the initial value problem for hyperbolic conservation laws. A novel immersed-boundary method for solving advection problems is presented. The immersed-boundary method, in general, is a method in which boundary conditions are indirectly incorporated into the governing equations. It has undergone numerous modifications, ever since its first introduction by Peskin in 1972 [1], and currently many varieties of it exist (see [2] for a review and the references therein for details). Immersed-boundary methods are very suitable for simulating flows around flexible, moving and/or complex bodies. Basically, the bodies of interest are just embedded in non-deforming Cartesian grids that do not conform to the shape of the body. The governing equations are modified to include the effect of the embedded boundaries.

Our approach uses a cell-centered finite-volume discretization. The governing partial differential equations are discretized using a standard finite-volume method away from the embedded body. Near the embedded body, a special finite-volume method is derived which takes the prescribed interior boundary conditions into account. Doing so, mesh (re)generation difficulties associated with body-fitted grids, are obviated; and, the underlying regular fixed grid allows us to use a simple data structure as well as simpler numerical schemes over a majority of the domain.

The outline of the paper is as follows. In § 2, the problem is described and some standard finite-volume results are presented. The special fluxes which take the effects of the embedded boundaries into account are derived in § 3; and in § 4, the temporal integration is explained. In § 5, some numerical results, based on the present approach, are given, and finally concluding remarks are presented in § 6.

---

2 Problem description

2.1 Model equation and target problems

The one-dimensional, linear advection equation is:

$$\frac{\partial c}{\partial t} + \frac{\partial f(c)}{\partial x} = 0, \qquad f(c) = u\,c, \tag{1}$$

where $c(x,t)$ is the scalar field and $f(c)$ is the flux function, which is linear. Equation (1) is a model of quantity $c(x,t)$ that is advected by the velocity u, which is constant, and which we assume to be positive. The independent variables x and t represent space and time, respectively. The generic domain of the solution is a one-dimensional rod, of length L. Here, we take the domain to be of unit length, $L = 1$, on the interval $x \in [0, 1]$.

The advection equation (1) is the simplest partial differential equation, but it is an important one, as it models fluid-flow equations. It is hyperbolic with a single set of characteristic lines. For a given initial solution $c(x, 0) = c_0(x)$, the exact solution of (1), at any location x and time t, can be computed by the method of characteristics, as $c(x,t) = c_0(x - ut)$. The initial data simply propagates unchanged with the velocity u.

Two initial solutions are considered, each with two interior, moving boundaries. The solution at the left and right of each interior boundary is prescribed. The two moving boundaries have arbitrary initial locations (x_1 and x_2, $x_1 \neq x_2$). The two solutions, in formulae, read:

$$c_0(x) = \begin{cases} 0, & \text{if } x_1 \leq x \leq x_2, \\ 1, & \text{elsewhere;} \end{cases} \quad \text{and} \quad c_0(x) = \begin{cases} 0, & \text{if } x_1 \leq x \leq x_2, \\ \frac{1 - \cos(2\pi x)}{2}, & \text{elsewhere.} \end{cases} \tag{2}$$

The initial solutions are able to distinctly rank out the different numerical schemes based on their accuracy. The cosine function in (2) exploits the advantage that higher-order accurate numerical schemes have in non-constant, smooth solution regions.

The model equation is approximated in a periodic domain, allowing us to time-step for as long as we want for a finite spatial domain.

Hence, by using the exact solution as a benchmark, numerous numerical schemes can be developed and tested for the one-dimensional, linear advection equation. Fixed-grid finite-volume methods for advection problems with interior, embedded moving boundaries are underdeveloped. No rigorous studies exist about numerical properties as accuracy and monotonicity. In this paper, some finite-volume methods for discontinuous moving interior boundary problems will be derived, analyzed and tested. The moving interior boundary conditions will be embedded in the fluxes in the direct neighborhood.

2.2 Finite-volume method and standard schemes

The unit domain is divided into N non-overlapping control volumes of uniform size, with the grid size being $h = 1/N$. A single node is located at the geometric centroid of the control volume and the cells are represented with nodal indices. The coordinates of the nodes are determined as $x_i = (i - \frac{1}{2})h$, $i = 1, 2, ..., N$. The coordinates of the cell faces are labeled by indices-with-fractions: $x_{i+\frac{1}{2}}$, $i = 1, 2, ..., N$.

Denoting the discrete solution in cell i, at time level n, as $c_i^n = c(x_i, t^n)$, which is assumed to be constant in that cell and at that time, the semi-discrete finite-volume form of (1) reads:

$$h\frac{\mathrm{d}c_i}{\mathrm{d}t} + \left(f_{i+\frac{1}{2}}^n - f_{i-\frac{1}{2}}^n\right) = 0. \tag{3}$$

Equation (3) is exact so far. It is going to be solved by approximating the fluxes at the cell faces and by time-stepping the temporal part.

The flux across cell face $i+\frac{1}{2}$, at time level n, is computed (dropping the time index n, for convenience) as $f_{i+\frac{1}{2}} = uc_{i+\frac{1}{2}}$, where $c_{i+\frac{1}{2}}$ is the cell-face state at $i+\frac{1}{2}$, which can be approximated in a

variety of ways. For example, for $u > 0$, $c_{i+\frac{1}{2}} = c_i$ and $c_{i+\frac{1}{2}} = c_i + \frac{1+\kappa}{4}(c_{i+1} - c_i) + \frac{1-\kappa}{4}(c_i - c_{i-1})$ are two classical cell-face states, computed with the first-order upwind scheme and van Leer's κ-scheme [3], respectively. Note that, with no embedded boundary in the neighborhood, $\kappa \in [-1, 1]$. For $\kappa = 1$ and -1, we have the second-order accurate central and fully upwind schemes, respectively. And for the unique value $\kappa = \frac{1}{3}$, we have a third-order net-flux accuracy in each cell.

The simplicity and monotonicity of the first-order upwind scheme are appealing, making it a robust scheme. However, it has strong numerical diffusion. On the other hand, the solutions of all κ-schemes exhibit wiggles in the vicinity of discontinuities. This recalls Godunov's theorem [4] which states that there is no linear scheme higher than first-order accurate, which is monotone. Several algorithms have been proposed in the literature that yield higher-order accurate solutions which are free from wiggles. Most of these algorithms exploit the inherent monotonicity of the first-order upwind scheme. The best known representatives of these algorithms are the limited schemes following Sweby's total-variation diminishing (TVD) theory [5].

The cell-face state at $i+\frac{1}{2}$ can be rewritten in the limited form as $c_{i+\frac{1}{2}} = c_i + \frac{1}{2}\phi(r_{i+\frac{1}{2}})(c_i - c_{i-1})$, where $\phi(r)$ is the limiter function and $r_{i+\frac{1}{2}} = \frac{c_{i+1}-c_i}{c_i-c_{i-1}}$ is its monotonicity argument. Here we specifically adopt the limiter proposed by Koren [6] as the standard limiter. It gives a monotone third-order accurate net flux in a cell by resembling the $\kappa = \frac{1}{3}$-scheme, and is defined as:

$$\phi(r) = \begin{cases} 0, & \text{if } r < 0; \\ 2\,r, & \text{if } 0 \leq r < \frac{1}{4}; \\ \frac{1}{3} + \frac{2}{3}\,r, & \text{if } \frac{1}{4} \leq r < \frac{5}{2}; \\ 2, & \text{otherwise.} \end{cases} \tag{4}$$

In the remainder of this paper, we will derive non-standard finite-volume methods, methods in which the interior boundary conditions are incorporated in the fixed-grid flux formulae. Before doing so, for later comparison purposes, we will show what the solutions are for the standard finite-volume discretizations described above, methods in which no embedded-boundary conditions are imposed, pure capturing methods, in fact. For the time integration, the three-stage Runge-Kutta scheme RK3b from [7] is employed. For both initial solutions given in (2), we consider the locations of the embedded bodies to be at $x_1 = \frac{1}{3}$ and $x_2 = \frac{2}{3}$. Furthermore, we take $u = 1$, and we compute the solution at $t = 1$, the time at which the solution has made a single full-period. For both the first-order upwind and the $\kappa = \frac{1}{3}$ (unlimited and limited) schemes, the computations are performed on a grid with 20 and 40 cells. The solutions are depicted in Figure 1. The time steps have been taken sufficiently small to ensure that in all cases the time discretization errors are negligible with respect to the spatial discretization errors.
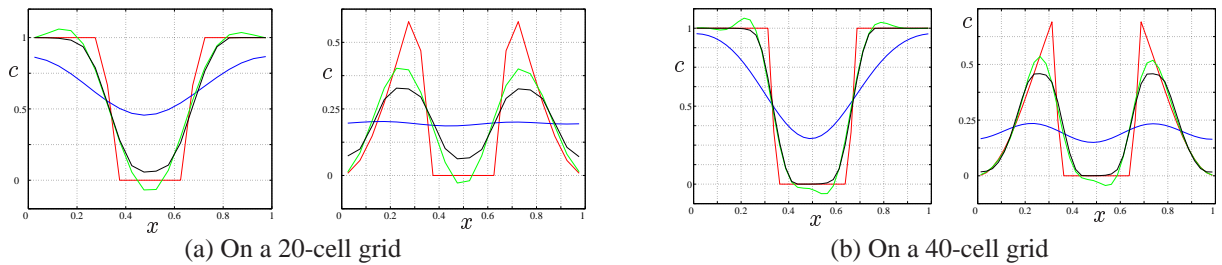

(a) On a 20-cell grid   (b) On a 40-cell grid

Figure 1: Standard finite-volume solutions after one full-period, for the initial solutions (2). Red: exact discrete, blue: first-order upwind, green: unlimited higher-order upwind-biased, and black: limited higher-order upwind-biased.

3   Fluxes with embedded moving-boundary conditions

3.1   Higher-order accurate embedded-boundary fluxes

The sharp discontinuities of the initial solutions (2) are considered as infinitely thin bodies going with the flow and the boundary conditions associated with these are embedded in the fixed-grid fluxes. We speak of embedded bodies (EBs). Here, the embedded-boundary conditions are user-specified and enforced to remain intact to the EB and unchanged at all times. The solution values on the left and right sides of the EB are designated as c_{EB}^l and c_{EB}^r, respectively (Figure 2).
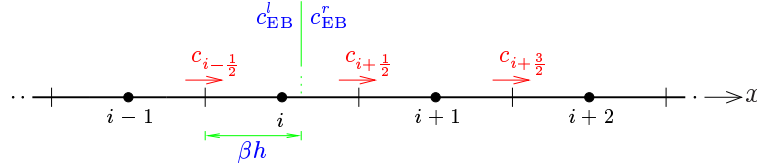

Figure 2: EB situated in cell i at time t, its associated solution values, and the affected cell-face states.

For an EB situated in cell i, with its coordinate $x_{\text{EB}} = x_{\text{EB}}(t)$ given, its relative position with respect to the left face of the cell is βh, see Figure 2, where $\beta \in [0, 1]$ is a (non-dimensional) parameter which is defined as:

$$\beta = \frac{x_{\text{EB}} - x_{i-\frac{1}{2}}}{h}. \tag{5}$$

So, $\beta = 0$ when the EB is at cell face $i-\frac{1}{2}$, $\beta = \frac{1}{2}$ when the EB is in the centroid i, and $\beta = 1$ when the EB is at cell face $i+\frac{1}{2}$.

There is no information flow across the EB. Fluxes on one side of the EB are all computed based on the information on that side of the EB and the additional interior boundary condition on the respective side. In general, when considering three-point upwind-biased interpolation for the fluxes, three cell-face states, viz. $c_{i-\frac{1}{2}}$, $c_{i+\frac{1}{2}}$ and $c_{i+\frac{3}{2}}$, are affected by the presence of a single EB (in cell i) and these are the cell-face states of interest that will be modified. These three cell-face states are computed such that the net fluxes in the neighboring cells are as accurate as possible. So far, it is assumed that two successive EBs are sufficiently far apart that a given flux is affected by only one EB. Recall that all but the affected fluxes are computed based on the standard κ-scheme discussed in § 2.2.

In principle, all the special cell-face states are written in terms of the blending parameter κ and are computed from optimally blended, three-point upwind-biased interpolation formulae. However, for cell-face state $c_{i+\frac{1}{2}}$, no upwind-biased interpolation formula can be derived as we do not draw information across the EB. Hence, no blending parameter to be optimized in the formula for $c_{i+\frac{1}{2}}$, and only non-equidistant central interpolation is applied to compute $c_{i+\frac{1}{2}}$, i.e.,

$$c_{i+\frac{1}{2}} = c_{\text{EB}}^r + \frac{2 - 2\beta}{3 - 2\beta}(c_{i+1} - c_{\text{EB}}^r). \tag{6}$$

In the formulae for $c_{i-\frac{1}{2}}$ and $c_{i+\frac{3}{2}}$, there will be blending parameters; $c_{i-\frac{1}{2}}$ and $c_{i+\frac{3}{2}}$ can be taken as optimally weighted averages of two-point central interpolation and two-point fully-upwind extrapolation.

The net fluxes of cells $i-1$, i, $i+1$ and $i+2$ are affected by the EB. Because only $c_{i-\frac{1}{2}}$ and $c_{i+\frac{3}{2}}$ allow for optimization, only two of the four aforementioned net cell-fluxes can be optimized for accuracy: either the net flux in cell $i-1$ or cell i, for $c_{i-\frac{1}{2}}$; and either the net flux in cell $i+1$ or cell $i+2$, for $c_{i+\frac{3}{2}}$.

For the accuracy optimizations, Taylor series expansions are used. Doing so, the net flux in cell i cannot be optimized due to the presence of the EB with its discontinuous solution behavior. Hence, the net flux in cell $i-1$ will be optimized for $c_{i-\frac{1}{2}}$. Secondly, for $c_{i+\frac{3}{2}}$, the net flux in cell $i+2$ will be optimized. The reason why the net flux in cell $i+2$ is optimized instead of that of cell $i+1$ is explained at the end of this subsection.

Deriving the three-point upwind-biased interpolation for $c_{i-\frac{1}{2}}$, in terms of the blending parameter $\kappa_{i-\frac{1}{2}}$, we get:

$$c_{i-\frac{1}{2}} = c_{i-1} + \frac{1}{1+2\beta}\frac{1+\kappa_{i-\frac{1}{2}}}{2}(c_{\mathrm{EB}}^l - c_{i-1}) + \frac{1-\kappa_{i-\frac{1}{2}}}{4}(c_{i-1} - c_{i-2}). \qquad (7)$$

Note that for $\beta = \frac{1}{2}$, the standard κ-scheme is restored from (7). Then writing the modified equation for cell $i-1$, introducing successive Taylor series expansions about the point $i-1$, and equating the leading term of the truncation error to zero, we get:

$$\kappa_{i-\frac{1}{2}} = \frac{7-6\beta}{9+6\beta}, \qquad \kappa_{i-\frac{1}{2}} \in \left[\frac{1}{15}, \frac{7}{9}\right]. \qquad (8)$$

Following the same procedure for $c_{i+\frac{3}{2}}$, i.e., taking:

$$c_{i+\frac{3}{2}} = c_{i+1} + \frac{1+\kappa_{i+\frac{3}{2}}}{4}(c_{i+2} - c_{i+1}) + \frac{2}{3-2\beta}\frac{1-\kappa_{i+\frac{3}{2}}}{4}(c_{i+1} - c_{\mathrm{EB}}^r), \qquad (9)$$

we get the highest accuracy in cell $i+2$, for:

$$\kappa_{i+\frac{3}{2}} = \frac{7-6\beta}{15-6\beta}, \qquad \kappa_{i+\frac{3}{2}} \in \left[\frac{1}{9}, \frac{7}{15}\right]. \qquad (10)$$

$\kappa_{i-\frac{1}{2}}$ and $\kappa_{i+\frac{3}{2}}$ according to (8) and (10) are well within the standard range $[-1, 1]$. They yield the most accurate net fluxes in cells $i-1$ and $i+2$; we have second-order (spatial) accuracy in these cells, with a maximum leading-term truncation-error coefficient of $\pm\frac{h^2}{18}$ and $\pm\frac{h^2}{36}$, respectively. These are dispersive terms and they diminish as the EB is in the immediate vicinity of the center of cell i. We get third-order accuracy in the respective cells when the EB is exactly at the center, i.e., for $\beta = \frac{1}{2}$, $\kappa_{i-\frac{1}{2}} = \kappa_{i+\frac{3}{2}} = \frac{1}{3}$.

The final formulae for the special cell-face states that are affected by the presence of an EB, in cell i, are summarized, in terms of the location parameter β, as:

$$c_{i-\frac{1}{2}} = c_{i-1} + \frac{8}{(3+6\beta)(3+2\beta)}(c_{\mathrm{EB}}^l - c_{i-1}) + \frac{1+6\beta}{18+12\beta}(c_{i-1} - c_{i-2}), \qquad (11\mathrm{a})$$

$$c_{i+\frac{1}{2}} = c_{\mathrm{EB}}^r + \frac{2-2\beta}{3-2\beta}(c_{i+1} - c_{\mathrm{EB}}^r), \qquad (11\mathrm{b})$$

$$c_{i+\frac{3}{2}} = c_{i+1} + \frac{11-6\beta}{30-12\beta}(c_{i+2} - c_{i+1}) + \frac{4}{(9-6\beta)(5-2\beta)}(c_{i+1} - c_{\mathrm{EB}}^r). \qquad (11\mathrm{c})$$

Finally, the reasons why the optimal $\kappa_{i+\frac{3}{2}}$ is obtained from the highest accuracy of the net flux in cell $i+2$, instead of that in cell $i+1$, are the following:

- $\kappa_{i+\frac{3}{2}}$ from the former case is well within the standard κ-range $[-1, 1]$ (see (10)), but from the later case, we get $\kappa_{i+\frac{3}{2}} \in [\frac{1}{3}, \frac{7}{5}]$.

- We get a third-order (spatial) accuracy in cell $i+2$ in the former case for $\beta = \frac{1}{2}$ (see (10)), but in the later case, we do not get this for any β.

- Noting the solution is discontinuous across an EB, from the former case, we have a dissipative leading-error term in cell $i+1$, which is the adjacent cell to cell i (where the EB is situated), and this makes the solution near the EB less prone to numerical oscillations. In the later case, however, we get the leading-error term in the same cell to be dispersive and this makes the solution near the EB to be more susceptible to numerical oscillations, numerical oscillations which may be hard to suppress because construction of a flux limiter for cell face $i+\frac{1}{2}$ is hard.

- In the former case, we get first-order (spatial) accuracy in cell $i+1$, and second-order accuracy in cell $i+2$; whereas, in the later case, we get second-order accuracy in cell $i+1$, and first-order accuracy in cell $i+2$. Therefore, the accuracy deterioration due to the presence of an EB in cell i is confined to the vicinity of the EB.

3.2 Spatial monotonicity domains and limiters

Recalling Godunov's work [4], all the linear higher-order fluxes, constructed earlier, may yield wiggles. And these wiggles may cause the solution c to be negative. If c is a physical quantity that should not become negative (say, density or temperature), this is undesirable. Therefore, a physically positive quantity should remain positive during the course of the entire solution process. Positivity of c can be achieved by carefully constraining or 'limiting' the advective fluxes calculated by the scheme. By limiting the fluxes, they may persist to be first-order accurate in some solution regions. For the cell-face states that are computed by the standard $\kappa = \frac{1}{3}$ scheme (§ 2.2), the standard $\kappa = \frac{1}{3}$ limiter (4) will be used.

In this section, special limiters will be introduced for the special EB-affected cell-face states $c_{i-\frac{1}{2}}$ and $c_{i+\frac{3}{2}}$ according to formulae (11a) and (11c). For cell face $i+\frac{1}{2}$, a regular monotonicity argument $r_{i+\frac{1}{2}}$ can not be defined, as a regular monitor uses two solution values upstream of cell faces. In this case, since we do not want to use solution values from the other side of the EB, and therefore not c_i, we have only one upstream solution, c_{EB}^r, too little to introduce the regular smoothness monitor. Therefore, $c_{i+\frac{1}{2}}$ will not be limited.

The formulae for $c_{i-\frac{1}{2}}$ and $c_{i+\frac{3}{2}}$ in (11) can be rewritten as:

$$c_{i-\frac{1}{2}} = c_{i-1} + \frac{1}{2}\tilde{\phi}(\tilde{r}_{i-\frac{1}{2}})(c_{i-1} - c_{i-2}) \quad \text{and} \quad c_{i+\frac{3}{2}} = c_{i+1} + \frac{1}{3-2\beta}\tilde{\phi}(\tilde{r}_{i+\frac{3}{2}})(c_{i+1} - c_{EB}^r), \quad (12a)$$

where:

$$\tilde{\phi}(\tilde{r}_{i-\frac{1}{2}}) = \frac{1+6\beta}{9+6\beta} + \frac{8}{9+6\beta}\tilde{r}_{i-\frac{1}{2}} \quad \text{and} \quad \tilde{\phi}(\tilde{r}_{i+\frac{3}{2}}) = \frac{4}{15-6\beta} + \frac{11-6\beta}{15-6\beta}\tilde{r}_{i+\frac{3}{2}}, \quad (12b)$$

and where:

$$\tilde{r}_{i-\frac{1}{2}} = \frac{2}{1+2\beta}\frac{c_{EB}^l - c_{i-1}}{c_{i-1} - c_{i-2}} \quad \text{and} \quad \tilde{r}_{i+\frac{3}{2}} = \frac{3-2\beta}{2}\frac{c_{i+2} - c_{i+1}}{c_{i+1} - c_{EB}^r}. \quad (12c)$$

The function $\tilde{\phi}(\tilde{r})$ will be constrained to yield monotonicity preserving schemes and to define the appropriate limiters. The argument $\tilde{r}$ measures the local monotonicity of the solution. Notice that for $\beta = \frac{1}{2}$, $\tilde{r}_{i-\frac{1}{2}}$ and $\tilde{r}_{i+\frac{3}{2}}$ reduce to the standard equidistant local successive solution-gradient ratios known from the theory of standard limiters.

To constrain $\tilde{\phi}(\tilde{r}_{i-\frac{1}{2}})$, enforcing the monotonicity requirements:

$$\frac{c_{i-\frac{1}{2}} - c_{i-\frac{3}{2}}}{c_{i-1} - c_{i-2}} \geq 0 \quad \text{and} \quad \frac{c_{EB}^l - c_{i-\frac{1}{2}}}{c_{EB}^l - c_{i-1}} \geq 0, \quad (13)$$

we get:

$$1 + \frac{1}{2}\tilde{\phi}(\tilde{r}_{i-\frac{1}{2}}) - \frac{1}{2}\frac{\phi(r_{i-\frac{3}{2}})}{r_{i-\frac{3}{2}}} \geq 0 \quad \text{and} \quad 1 - \frac{1}{1+2\beta}\frac{\tilde{\phi}(\tilde{r}_{i-\frac{1}{2}})}{\tilde{r}_{i-\frac{1}{2}}} \geq 0 \quad (14)$$

respectively. The standard limiter $\phi(r)$ already satisfies $1 - \frac{1}{2}\frac{\phi(r)}{r} \geq 0$, $\forall r$. Therefore, the above (in)equalities reduce to:

$$\tilde{\phi}(\tilde{r}_{i-\frac{1}{2}}) \geq 0, \ \forall \tilde{r}_{i-\frac{1}{2}} \quad \text{and} \quad \tilde{\phi}(\tilde{r}_{i-\frac{1}{2}}) \leq (1+2\beta)\tilde{r}_{i-\frac{1}{2}}, \ \forall \tilde{r}_{i-\frac{1}{2}} > 0. \quad (15)$$

Similarly, to constrain $\tilde{\phi}(\tilde{r}_{i+\frac{3}{2}})$, enforcing the monotonicity requirements:

$$\frac{c_{i+\frac{3}{2}} - c_{i+\frac{1}{2}}}{c_{i+1} - c_{EB}^r} \geq 0 \quad \text{and} \quad \frac{c_{i+\frac{5}{2}} - c_{i+\frac{3}{2}}}{c_{i+2} - c_{i+1}} \geq 0, \quad (16)$$

we get as restrictions for $\tilde{\phi}(\tilde{r}_{i+\frac{3}{2}})$:

$$\tilde{\phi}(\tilde{r}_{i+\frac{3}{2}}) \geq -1 \quad \text{and} \quad \frac{\tilde{\phi}(\tilde{r}_{i+\frac{3}{2}})}{\tilde{r}_{i+\frac{3}{2}}} \leqq 2, \quad \forall \tilde{r}_{i+\frac{3}{2}}. \tag{17}$$

The (in)equalities (15) and (17) partially define the spatial monotonicity domains for the special limiter functions $\tilde{\phi}(\tilde{r}_{i-\frac{1}{2}})$ and $\tilde{\phi}(\tilde{r}_{i+\frac{3}{2}})$. Upper bounds for both limiters are still to be derived in § 4.2.

4 Time integration

4.1 Temporal discretization

Semi-discrete equation (3), after substituting the appropriate discretizations for the spatial operator, is compactly written as:

$$\frac{\mathrm{d}c_i}{\mathrm{d}t} = -\frac{u}{h}(c_{i+\frac{1}{2}} - c_{i-\frac{1}{2}}) \equiv F(c). \tag{18}$$

Equation (18) can be integrated in time, using a variety of explicit and implicit time-integration methods. Here, only two explicit schemes are considered: the Forward Euler and RK3b [7] schemes. The later gives a third-order accuracy in time.

For the Forward Euler method, (18) becomes:

$$c_i^{n+1} = c_i^n + \tau F(c^n) \equiv c_i^n - \nu(c_{i+\frac{1}{2}}^n - c_{i-\frac{1}{2}}^n), \tag{19}$$

where $\nu = \frac{u\tau}{h}$ is the CFL number, and τ the time step. Similarly, for the RK3b scheme, we have:

$$c_i^{n+1} = c_i^n + \frac{1}{6}(R_1 + R_2 + 4R_3), \tag{20a}$$

where the R_j's ($j = 1, 2, 3$) are internal vectors that are computed as:

$$R_1 = \tau F(c^n), \quad R_2 = \tau F(c^n + R_1) \quad \text{and} \quad R_3 = \tau F(c^n + \frac{1}{4}R_1 + \frac{1}{4}R_2). \tag{20b}$$

4.2 Monotonicity condition and time step

Higher-order accurate solutions of time-dependent problems may exhibit under- and over-shoots near discontinuities, as they evolve in time. The limited numerical flux conditions, as derived in § 3.2, are still insufficient to guarantee monotonicity during time integration. Harten's theorem [8] provides additional conditions that are necessary for the convergence of the fully-discrete solutions to the exact, monotone solutions. These conditions define the upper bounds for the limiters $\tilde{\phi}(\tilde{r}_{i-\frac{1}{2}})$ and $\tilde{\phi}(\tilde{r}_{i+\frac{3}{2}})$.

The theorem in [8] states, any consistent scheme for a conservation law written in the conservative form:

$$c_i^{n+1} = c_i^n - D_{i-\frac{1}{2}}^- \left(c_i^n - c_{i-1}^n \right) + D_{i+\frac{1}{2}}^+ \left(c_{i+1}^n - c_i^n \right), \tag{21}$$

where the D's are solution-dependent coefficients, is total-variation diminishing (TVD) if, for all i:

$$D_{i+\frac{1}{2}}^{\pm} \geq 0, \tag{22a}$$

$$D_{i+\frac{1}{2}}^- + D_{i+\frac{1}{2}}^+ \leq 1. \tag{22b}$$

To fully constrain the limiters $\tilde{\phi}(\tilde{r}_{i-\frac{1}{2}})$ and $\tilde{\phi}(\tilde{r}_{i+\frac{3}{2}})$, we consider the Forward Euler scheme and write the fully discrete equations, in the form (21), for cell $i-1$, and cells $i+1$ and $i+2$, respectively. After enforcing conditions (22), we then get the bounds of the domains as:

$$0 \leq \tilde{\phi}(\tilde{r}_{i-\frac{1}{2}}) \leq \frac{2}{\nu} - 2, \quad -1 \leq \tilde{\phi}(\tilde{r}_{i+\frac{3}{2}}) \leq \frac{3 - 2\beta}{\nu} - 1 \quad \text{and} \quad 4 - \frac{2}{\nu} \leq \frac{\tilde{\phi}(\tilde{r}_{i+\frac{3}{2}})}{\tilde{r}_{i+\frac{3}{2}}} \leq 2. \tag{23}$$

Note that the above three bounds that contain ν follow from the requirement (22b). The other three bounds (0, -1 and 2) follow from the requirement (22a), which is analogous to the monotonicity requirement already considered in § 3.2. Concerning the newly derived ν-dependent bounds ($\frac{2}{\nu} - 2$, $\frac{3-2\beta}{\nu} - 1$ and $4 - \frac{2}{\nu}$), note that the choice $\nu = 1$ – which, as is known, is the stability bound for Forward Euler – yields $\tilde{\phi}(\tilde{r}_{i-\frac{1}{2}}) = 0$ and $\tilde{\phi}(\tilde{r}_{i+\frac{3}{2}}) = \tilde{r}_{i+\frac{3}{2}}$. Hence, with $\nu = 1$, the second-order accuracy requirements $\tilde{\phi}(\tilde{r}_{i-\frac{1}{2}} = 1) = 1$ and $\tilde{\phi}(\tilde{r}_{i+\frac{3}{2}} = 1) = 1$ cannot be satisfied for both limiters. $\nu = \frac{1}{2}$ is the maximum value that still allows for $\tilde{\phi}(\tilde{r}_{i+\frac{3}{2}} = 1) = 1$ for $\beta = 1$.

For the case $\beta = \frac{1}{2}$ and $\nu < \frac{1}{2}$, possible limiters satisfying the requirements (23) are depicted in Figure 3.
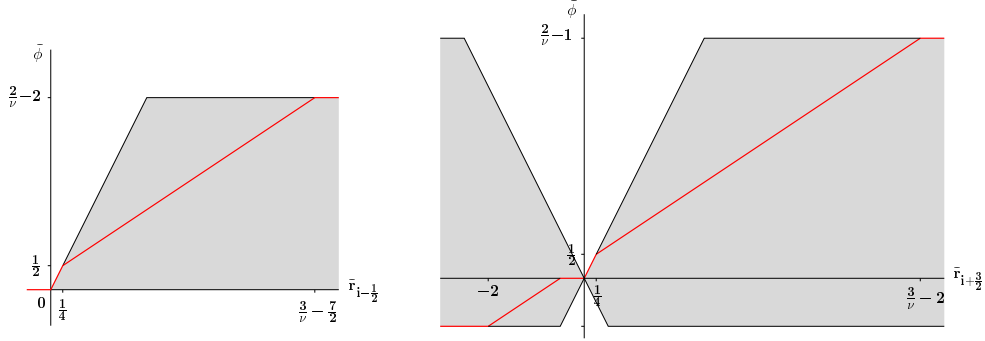

Figure 3: Typical EB-sensitive limiters and the corresponding monotonicity domains for the special cell-face states $c_{i-\frac{1}{2}}$ (left) and $c_{i+\frac{3}{2}}$ (right), for $\beta = \frac{1}{2}$.

4.3 Local adaptivity in time

Consider the stencil in the (x, t)-plane in Figure 4. The EB is situated in cell i at t^n in such a way that it migrates to the next cell $i+1$. Apparently, the solutions c_i^n and c_{i+1}^n are updated, in Forward Euler, using the modified cell-face states $c_{i-\frac{1}{2}}^n$, $c_{i+\frac{1}{2}}^n$ and $c_{i+\frac{3}{2}}^n$. However, as the EB crosses the cell face at $x_{i+\frac{1}{2}}$, there is an abrupt change in the state at this face. That is, before the crossing, the state at this cell face is computed based on the data to the right of the EB; whereas, after the crossing, it is computed based on the data to the left of the EB. The two updated solutions c_i^{n+1} and c_{i+1}^{n+1}, which are mainly affected by this particular cell-face state, need to 'feel' the reversal, more in particular the abrupt change in $c_{i+\frac{1}{2}}$.
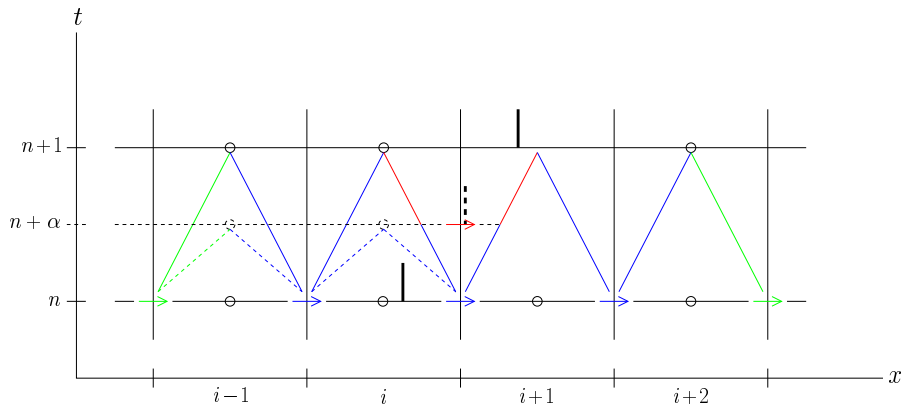

Figure 4: Stencil for local adaptivity in time. The standard, modified and the intermediate cell-face states are designated in green, blue, and red, respectively.

Time adaptivity is introduced by first computing the time fraction α at which the EB crosses the cell face at $x_{i+\frac{1}{2}}$, as:

$$\alpha = \frac{x_{i+\frac{1}{2}} + \epsilon - x_{\text{EB}}^n}{u\,\tau}, \qquad \alpha \in (0, 1), \tag{24}$$

where x_{EB}^n is the location of the EB at time level t^n. Note that the EB is placed at infinitesimal distance ϵ off $x_{i+\frac{1}{2}}$, in the direction of the flow. Then, after updating the solution values c_{i-1}^n and c_i^n to time level $n+\alpha$, the intermediate cell-face state $c_{i+\frac{1}{2}}^{n+\alpha}$ is computed. Finally, the cell-face state $c_{i+\frac{1}{2}}^n$ is recomputed as the weighted average:

$$c_{i+\frac{1}{2}}^n := \alpha c_{i+\frac{1}{2}}^n + (1 - \alpha) c_{i+\frac{1}{2}}^{n+\alpha}. \tag{25}$$

Then using the time-adapted cell-face state, solution updating is continued everywhere with the regular time step τ.

For RK3b, we do not yet resort to the temporal local-adaptivity procedure devised above. We instead split the regular time step τ into smaller time steps, depending on the number of EBs crossing cell faces, and update the intermediate solutions everywhere. For instance, for a single EB crossing a cell face, we divide τ into two smaller time steps $\alpha\tau$ and $(1 - \alpha)\tau$.

5   Numerical examples

We present numerical results to validate the immersed-boundary approach presented in this work. We take the same data as in § 2.2, i.e., the same initial solutions (2), initial EB locations $x_1 = \frac{1}{3}$ and $x_2 = \frac{2}{3}$, $u = 1$, and $t_{\max} = 1$, on a grid of 20 and 40 cells.

The results obtained, shown in Figure 5, are remarkably accurate. The results show a significant improvement in resolution, without much computational overhead, over those computed using the standard methods, Figure 1. For the more discriminating initial solution (the cosine-cavity), the numerical results of the limited higher-order upwind-biased schemes are slightly deficient at the peripheries. This is due to the property of limiters that they clip physically relevant extrema. Apparently, the deficiency becomes smaller with decreasing mesh width.

6   Conclusion

The essence of the present approach is that moving bodies are embedded in a regular fixed grid and specific fluxes in the vicinity of the embedded boundary are intelligently computed in such a way that they accommodate the boundary conditions valid on the moving body. Then, over the majority of the domain, where we do not have influence of the embedded bodies, we can readily use standard methods on the underlying regular fixed grid. Excellent results are achieved, without much computational overhead. We foresee that the numerical methods introduced here can readily be extended to higher-dimensional, more practical and complicated problems, for instance the unsteady, incompressible Euler and Navier-Stokes equations.

References

[1] C.S. Peskin. Flow patterns around heart valves: a numerical method. *J. Comput. Phys.*, 10:252–271, 1972.

[2] R. Mittal and G. Iaccarino. Immersed boundary methods. *Ann. Rev. Fl. Mech.*, 37:239–261, 2005.

[3] B. van Leer. *Upwind-difference methods for aerodynamic problems governed by the Euler equations*. Lectures in Appl. Math., 22 - Part 2, Amer. Math. Soc., Providence, RI, 1985.

[4] S.K. Godunov. *Math. Sb.*, 44:271–306, 1959.

[5] P. Sweby. High resolution schemes using flux limiters for hyperbolic conservation laws. *SIAM J. Num. Anal.*, 21:995–1011, 1984.

[6] B. Koren. A robust upwind finite-volume method for advection, diffusion and source terms. In C.B. Vreugdenhil and B. Koren, editors, *Notes on Num. Fl. Mech.,* 45, Vieweg, Braunschweig, 1993.

[7] W. Hundsdorfer, B. Koren, M. van Loon, and J.G. Verwer. A positive finite-difference advection scheme. *J. Comput. Phys.*, 117:35–46, 1995.

[8] A. Harten. On a class of high resolution total-variation-stable finite-difference schemes. *SIAM J. Num. Anal.*, 21:1–23, 1984.
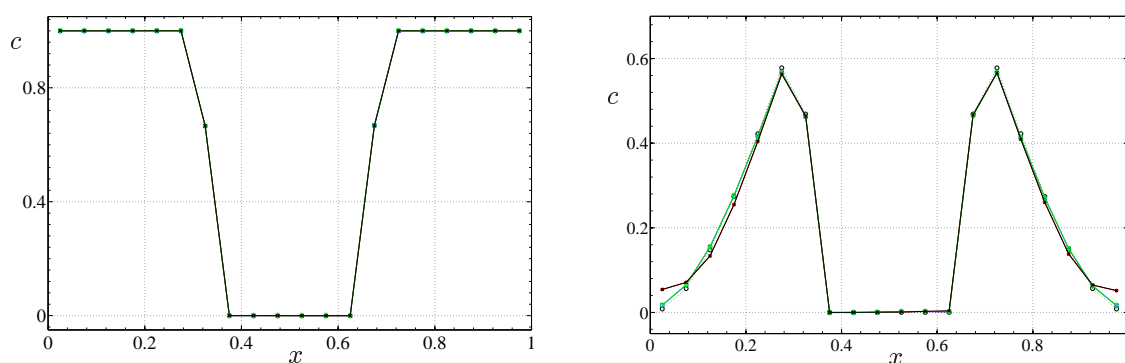
(a) On a 20-cell grid
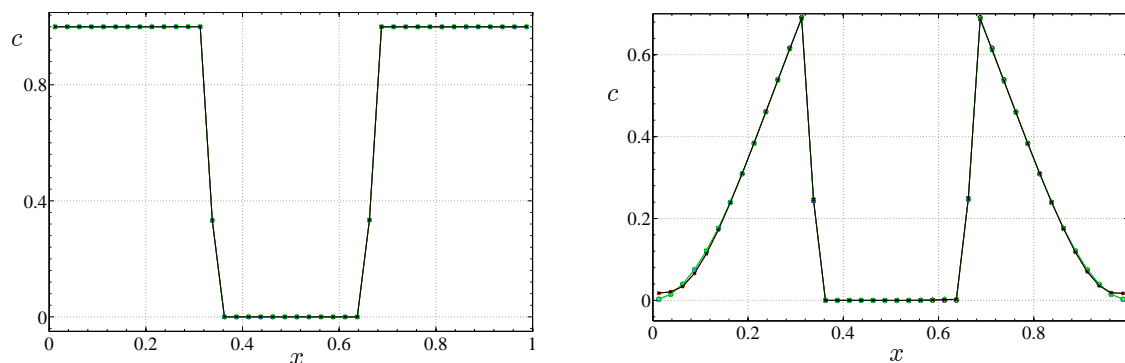
(b) On a 40-cell grid

Figure 5: Immersed-boundary solutions after one full-period, for the initial solutions (2). ○: exact discrete, □: unlimited higher-order upwind-biased with Forward Euler, ∗: limited higher-order upwind-biased with Forward Euler, ◇: unlimited higher-order upwind-biased with RK3b, ×: limited higher-order upwind-biased with RK3b.